Kinetic ballooning mode turbulence in low-average-magnetic-shear equilibria

I.J. McKinney[a], M.J. Pueschel[b,c,d], B.J. Faber[a], C.C. Hegna[a,f],

A. Ishizawa[e], and P.W. Terry[f]

[a] *Department of Engineering Physics, University of Wisconsin-Madison, Madison, Wisconsin 53706, USA*

[b] *Eindhoven University of Technology, 5600 MB Eindhoven, The Netherlands*

[c] *Dutch Institute For Fundamental Energy Research, 5612 AJ Eindhoven, The Netherlands*

[d] *Institute for Fusion Studies, The University of Texas at Austin, Austin, Texas 78712, USA*

[e] *Graduate School of Energy Science, Kyoto University, Uji, Kyoto, 611-0011, Japan*

[f] *Department of Physics, University of Wisconsin-Madison, Madison, Wisconsin 53706, USA*

Abstract

Kinetic-ballooning-mode (KBM) turbulence is studied via gyrokinetic flux-tube simulations in three magnetic equilibria that exhibit small average magnetic shear, the Helically Symmetric eXperiment (HSX), the helical-axis Heliotron-J, and a circular tokamak geometry. For HSX, the onset of KBM being the dominant instability at low wavenumber occurs at a critical value of normalized plasma pressure $\beta_{\mathrm{crit}}^{\mathrm{KBM}}$ that is an order of magnitude smaller than the magnetohydrodynamic (MHD) ballooning limit $\beta_{\mathrm{crit}}^{\mathrm{MHD}}$ when a strong ion temperature gradient is present. However, $\beta_{\mathrm{crit}}^{\mathrm{KBM}}$ increases and approaches the MHD ballooning limit as the ion temperature gradient tends to zero. For these configurations, $\beta_{\mathrm{crit}}^{\mathrm{KBM}}$ also increases as the magnitude of the average magnetic shear increases, regardless of the sign of the normalized magnetic shear. Simulations of Heliotron-J and a circular axisymmetric geometry display behavior similar to HSX with respect to $\beta_{\mathrm{crit}}^{\mathrm{KBM}}$. Despite large KBM growth rates at long wavelengths in HSX, saturation of KBM turbulence with $\beta > \beta_{\mathrm{crit}}^{\mathrm{KBM}}$ is achievable in HSX and results in lower heat transport relative to the electrostatic limit by roughly a factor of five. Nonlinear simulations also show that KBM transport dominates the dynamics when KBMs are destabilized linearly, even if KBM growth rates are subdominant to ITG growth rates.

1 Introduction

The stellarator as a fusion reactor concept is qualitatively different from the tokamak due to the inherently three-dimensional nature of the magnetic field. This added flexibility allows the stellarator approach to circumvent the need for toroidal plasma current to provide the confining poloidal magnetic field, meaning stellarators are less prone to potentially destructive plasma-current-driven instabilities [18]. One consequence of this improved magnetohydrodynamic (MHD) behavior is the potential for robust high-β operation, where $\beta = 8\pi p/B_0^2$ is the normalized plasma pressure, p is the electron pressure, and B_0 is the magnetic field strength, without the danger of current-driven instabilities. Even in the absence of large-scale MHD instability, the system may exhibit small-scale kinetic ballooning modes (KBMs), which could conceivably drive large energy and particle fluxes and thus be problematic for high-β operation of stellarators [1, 2, 30]. The purpose of this work is to expand on previous analyses of KBM instability and turbulence by probing the properties of these modes in stellarator equilibria with low average magnetic shear $\hat{s} = -(r/\iota\!\!\!{-})d\iota\!\!\!{-}/dr$, where $\iota\!\!\!{-}$ is the rotational transform and r is a radial coordinate labeling flux surfaces. Low average magnetic shear $\hat{s}$ is a notable design feature of some classes of neoclassical-transport-optimized stellarators such as HSX. A deeper understanding of KBM saturation in such configurations will aid in the optimization of low-$\hat{s}$ equilibria with respect to finite-β turbulent transport.

Neoclassical transport governs confinement in the classical stellarator. However, this issue can be quelled by ensuring that bounce-averaged particle excursions from a given flux surface during a banana orbit nearly vanish [6, 40]. There are a number of ways to reduce stellarator neoclassical transport to tokamak-like levels, such as quasi-symmetry [43, 53] or quasi-isodynamicity [39, 45], both of which are subsets of quasi-omnigeneity [21, 66]. Magnetic configurations with sufficiently-minimized neoclassical cross-field diffusion are dominated by anomalous transport [8, 26, 62]. Drift-wave turbulence is a primary candidate to explain anomalous transport in these configurations. Drift waves exist in a variety of types such as ion-temperature-gradient (ITG) modes [28, 38, 41, 55, 64, 65], trapped-electron modes [13, 14, 16, 34], or kinetic ballooning modes [2, 4, 12, 36, 50, 52, 58, 59].

KBMs are electromagnetic modes, as they require fluctuations in the magnetic field. Typically, the onset of KBM-driven turbulent transport is associated with breaching the ideal MHD ballooning stability boundary [50, 52, 56, 57]. It has been shown that ion magnetic drifts can introduce an additional physical effect not present in simple MHD modeling in the small-perpendicular-wavelength limit [1, 36]. Specifically, coupling between the KBM and thermal ions provides additional free energy to the mode. This resonant effect arises from non-adiabatic contributions to the ion density fluctuations in a kinetic treatment of the governing equations [24, 25]. This effect can be qualitatively captured in a two-fluid treatment of the system, suggesting that the mode is of a reactive type since the kinetic treatment is unnecessary for qualitative purposes [24].

In the present work, the focus lies on the $\beta_{\mathrm{crit}}^{\mathrm{KBM}}$ value at which KBM becomes the most unstable microinstability; for a discussion of different threshold definitions, see [52]. An analysis of various Wendelstein 7-X (W7-X) equilibria [2], an optimized quasi-omnigenous stellarator, with respect to KBMs suggests both that, for sufficiently large β, peak KBM growth rates occur as $k_y \to 0$ for a number of physically-relevant parameter regimes and that the critical β at which KBMs become unstable is on the order of $\beta_{\mathrm{crit}}^{\mathrm{KBM}} \approx 1\%$, depending on the specific equilibrium. It is also shown in the same analysis that, in low-average-magnetic-shear W7-X configurations, KBMs can be destabilized before the ideal MHD limit $\beta_{\mathrm{crit}}^{\mathrm{MHD}}$. As will be shown here, this KBM threshold can be much lower than the MHD threshold $\beta_{\mathrm{crit}}^{\mathrm{MHD}}$, with $\beta_{\mathrm{crit}}^{\mathrm{KBM}} \approx 0.2\%$ in the Helically Symmetric eXperiment (HSX, a quasi-helically symmetric stellarator) over a range of wavelengths, raising the possibility that such configurations exhibit poor KBM turbulence and confinement properties. However, it is shown here that the saturated nonlinear heat flux is greatly reduced relative to the electrostatic ITG case when $\beta > \beta_{\mathrm{crit}}^{\mathrm{KBM}}$. This implies that expectations based on linearly-calculated $\beta_{\mathrm{crit}}^{\mathrm{KBM}}$ values, e.g., that nonlinear heat fluxes tend to increase for $\beta > \beta_{\mathrm{crit}}^{\mathrm{KBM}}$, do not accurately account for critical nonlinear dynamics.

With the goal of developing a better understanding of the relationship between the magnetic geometry and $\beta_{\mathrm{crit}}^{\mathrm{KBM}}$, the gyrokinetic turbulence code Gene is used here to perform electromagnetic nonlinear gyrokinetic local flux-tube simulations [33], (see http://www.genecode.org for code details and access). This paper is organized as follows. Section 2 introduces both the simulation framework for the present work and details regarding the three magnetic geometries. In Sec. 3, linear and nonlinear electromagnetic simulations of KBMs and analyses thereof are presented. Section 4 will show the scaling of $\beta_{\mathrm{crit}}^{\mathrm{KBM}}$ with the average magnetic shear and the normalized ion temperature gradient and the similarities in linear KBM results between

HSX, Heliotron-J, and a circular tokamak. Lastly, conclusions are given in Sec. 5.

2 Simulation approach and magnetic geometries

The gyrokinetic code Gene [33] is used in this work to investigate KBM and ITG turbulence via flux-tube simulations of low-average-magnetic-shear equilibria, namely HSX, the helical-axis Heliotron-J (H-J) [44], and a circular tokamak geometry. Gene solves a system of coupled equations that consists of the Vlasov equation, the Poisson equation, and Ampère's Law while taking advantage of the increased computational efficiency provided by gyro-averaging the orbits of charged particles in a strong magnetic guide field [7]. For the full set of equations, see [51]. Gene uses a five-dimensional phase space in which the coordinate system consists of the x (radial), y (binormal), z (parallel to $\mathbf{B}_0$), $v_\parallel$ (parallel velocity space), and μ (perpendicular velocity space) directions. There is both a box size L and a resolution n for each direction. For the nonlinear HSX calculation presented here, the resolutions, box sizes, and hyperdiffusion coefficients are the following: $N_x = 128$, $N_y = 96$, $N_z = 512$, $N_{v\parallel} = 32$, $N_\mu = 8$, $L_y = 251.3\rho_\mathrm{s}$ (corresponding to $k_y^\mathrm{min}\rho_\mathrm{s} = 0.025$), $L_x = 217.6\rho_\mathrm{s}$, $N_\mathrm{pol} = 4$, $D_z = 8$, and $D_{v\parallel} = 2$, where $\rho_\mathrm{s} = c_\mathrm{s} m_\mathrm{i}/(eB)$ is the ion sound gyroradius, N_pol is the number of poloidal turns, D_z is the the parallel real-space hyperdiffusion coefficient, and $D_{v\parallel}$ is the parallel velocity-space hyperdiffusion coefficient [48]. Numerical convergence studies were performed, including for N_pol, to ensure that results presented here are numerically converged. Due to the significant extent along the field line of the KBMs studied in this work, $N_\mathrm{pol} = 4$ is required to achieve convergence [17]. If underresolved in N_pol, artificial reinforcement of the KBMs via the parallel boundary condition is possible, yielding unphysical results. This is consistent with previous work regarding TEMs in HSX and with recent studies of a tokamak geometry [5, 17]. Lastly, we do not include either parallel magnetic field fluctuations or collisions.

The MHD equilibrium solver VMEC [27] is used to generate the HSX and H-J equilibria, which are subsequently processed using the GIST code [63]. The coordinates are centred at the specified normalized toroidal magnetic flux $s_0 = \Psi/\Psi(a) = (r/a)^2$, where $\Psi(a)$ is the toroidal flux at the plasma boundary and a is the effective minor radius. Details pertaining to the specifics of low-$\hat{s}$ flux-tube geometries can be found in [17, 38] (HSX) and [29] (H-J). All three configurations have comparable values of the average magnetic shear $\hat{s}$ along any given field line. As will be shown in this work, the average magnetic shear plays a critical role in determining $\beta_{\text{crit}}^{\text{KBM}}$, beyond the threshold prediction from MHD.

The magnetic equilibria used in this work are as follows. HSX is a four-field-period stellarator, where the number of field periods is defined as the number of times the magnetic geometry repeats per one toroidal transit, with aspect ratio $A = R_0/a \approx 10$, where R_0 is the major radius, mean magnetic field $\langle B_0 \rangle \approx 1$ T, and low average magnetic shear $\hat{s} \approx -0.05$ at $s_0 = 0.5$. The major radius R_0 (minor radius a) of HSX is approximately 1.2 m (0.12 m). The HSX flux tube used throughout this work is centred at the outboard midplane, corresponding to $\alpha = 0$, where $\alpha = \theta - \iota\zeta$ is a field-line label and θ and ζ are the poloidal and toroidal angles in PEST coordinates, respectively, where PEST coordinates are a straight field-line coordinate system [20]. It should also be noted that HSX is not optimized for a specific β, and therefore the HSX configuration used is given by the vacuum case with $\beta = 0$. This choice, however, is independent of the β used in GENE. Investigation into the effect of including self-consistent, finite equilibrium β values was performed, and it was found that changing the equilibrium β does not significantly affect the results presented below. Figure 4, a plot of growth rate and real frequency spectra of HSX using both a $\beta = 0$ equilibrium and a self-consistent $\beta = 0.48\%$ equilibrium, highlights that there is no significant difference between the vacuum and finite-β cases. As a result, the ∇B and curvature κ drifts are taken to be the same in this work, as is consistent with a $\beta = 0$ equilibrium. The H-J configuration used in this work has an equilibrium $\beta \approx 0.03\%$, four field periods, aspect ratio $A \approx 7.3$, mean magnetic field $\langle B_0 \rangle \approx 1.35$ T, and average magnetic shear $\hat{s} \approx 0.028$, which is a factor of two smaller than HSX and of opposite sign, at $s_0 = 0.5$. The major radius R_0 (minor radius a) of H-J is 1.18 m (0.162 m). As was the case for HSX, the $\alpha = 0$ flux tube is employed for H-J in this work. It should be reiterated that H-J is not a quasi-symmetric stellarator. Lastly, an $\hat{s}$-α geometry, corresponding to a tokamak with circular flux surfaces, is used to investigate KBM dynamics in an axisymmetric system for comparison [12]. A value of average magnetic shear $\hat{s} = -0.052$ is used throughout, as is a self-consistent (with β and the pressure gradients) $\alpha_{\text{MHD}} = \iota^{-2}(R_0/L_n)[\beta_{\text{e}}(1+\eta_{\text{e}}) + \beta_{\text{i}}(1+\eta_{\text{i}})]$, where L_n and $\eta_{(\text{i,e})}$ are the density gradient scale length and the ratio of the (ion, electron) temperature gradient to the density gradient, respectively. It should be noted that since a negative value of $\hat{s}$ is used, this tokamak equilibrium is stable to ideal MHD ballooning, $\beta_{\text{crit}}^{\text{MHD}} \to \infty$ [3, 19].

3 Electromagnetic ITG and KBM turbulence

3.1 Linear eigenmodes in low-$\hat{s}$ configurations

Typically, as β increases, the normalized ITG growth rates γ in units of c_s/a, where c_s is the sound speed, steadily decrease [15, 35, 47]. This is known as finite-β ITG stabilization, or linear electromagnetic stabilization. The mechanism by which this stabilization occurs is the coupling between the ITG mode and the shear Alfvén wave. This efficiently transfers energy out of the ITG mode, reducing its growth. Alterations of the ion Landau resonance due to finite-equilibrium-β ∇B modifications from the bending of perturbed field lines can also play a role in the stabilization [32]. This reduction in growth rate will tend to reduce the nonlinear heat flux, but additional physics can also impact the dynamics.

Another mechanism which affects ITG transport levels as β increases is nonlinear electromagnetic stabilization [50, 52, 60, 61]. As β increases, one observes a reduction in nonlinear heat flux that is greater than the reduction in linear growth rates or quasilinear fluxes. As has been shown in Refs. [60, 61], the difference between the (quasi-)linear and nonlinear reduction stems from changes in the efficiency of zonal-flow-mediated energy transfer to stable modes. This effect has been shown to be active in a range of configurations, both of tokamak and stellarator type. It has also been demonstrated that the inclusion of a self-consistent Shafranov shift can eliminate nonlinear electromagnetic stabilization for different, specific parameter regimes [31].

The physical mechanism underlying KBM destabilization is the following. As with most microinstabilities, KBMs are destabilized when the driving force associated with the pressure gradient is sufficiently strong in the bad curvature region to overcome the stabilizing force from the magnetic field [11]. More specific to KBMs, the modifications to magnetic drifts by β-induced magnetic fluctuations result in destabilizing effects when a kinetic treatment is applied to the governing equations. This is due to a resonance between the KBM and thermal ions, giving the KBM an additional free energy source.

For the cases studied here, the dominant eigenmode for $\beta < \beta_\mathrm{crit}^\mathrm{KBM}$ is ITG, whose growth rate decreases with β. For $\beta \geq \beta_\mathrm{crit}^\mathrm{KBM}$, KBM has a larger growth rate than the ITG mode with the growth rate increasing rapidly with β. This critical value $\beta_\mathrm{crit}^\mathrm{KBM}$ is generally on the order of a percent in standard tokamaks and is comparable to the ideal MHD ballooning β limit for physically-relevant gradient values, see [30, 50, 52].

However, $\beta_{\rm crit}^{\rm KBM}$ is not always close to $\beta_{\rm crit}^{\rm MHD}$ and is, in general, a complicated function of the magnetic geometry.

Before presenting analyses of nonlinear simulations, the behavior and scaling of linear instability will be elucidated, for both dominant and subdominant eigenmodes. Typically, ITG and KBM growth rates decrease and increase, respectively, as β increases. Figure 1 highlights this behavior in HSX at normalized binormal wavenumber $k_y \rho_{\rm s} = 0.6$. Henceforth, normalized wavenumbers are denoted $k_y \rho_{\rm s} \rightarrow k_y$. The normalized gradients, β, and the temperature ratio used in these calculations and throughout this work are $a/L_{T{\rm i}} = 3$ and $a/L_{T{\rm e}} = a/L_n = 1$, $\beta = 0.48\%$, and $T_{\rm i}/T_{\rm e} = 1$, respectively, unless otherwise stated. Note the factor-of-three reduction in the ITG growth rate as β increases before the KBM becomes dominant. This significant reduction in ITG growth rates is not observed for all values of k_y, as evidenced by Fig. 2, where at $k_y = 0.1$ there is no significant reduction in γ before KBMs become dominant for either the $N_{\rm pol} = 1$ or the $N_{\rm pol} = 4$ case. This is partially due to the fact that, in the $k_y = 0.1$ case, the KBM becomes dominant at a small critical normalized plasma pressure $\beta_{\rm crit}^{\rm KBM} \approx 0.18\%$ versus $\beta_{\rm crit}^{\rm KBM} \approx 2.2\%$ for the $k_y = 0.6$ case. Also note that $N_{\rm pol} = 4$ is required to achieve convergence, as elongated eigenmodes can artifically self-reinforce via the parallel boundary condition.

The scaling of $\beta_{\rm crit}^{\rm KBM}$ with k_y is presented in Fig. 3 for both HSX (blue squares) and NCSX (black triangles), a quasi-axisymmetric stellarator configuration optimized for operation at $\beta \approx 4.2\%$ [42] with $\hat{s} \approx -0.5$ at $s_0 = 0.5$. For HSX, $\beta_{\rm crit}^{\rm KBM}$ is small relative to the ideal MHD ballooning limit $\beta_{\rm crit}^{\rm MHD}$, and considerably smaller than the high-$\hat{s}$ NCSX analog where $\beta_{\rm crit}^{\rm KBM}$ is comparable to $\beta_{\rm crit}^{\rm MHD}$. The normalized gradients and temperature ratio used in the NCSX calculations are the same as were used for HSX. The ideal ballooning limit $\beta_{\rm crit}^{\rm MHD}$ is also shown as a horizontal dashed line for each configuration. The NCSX curve smoothly approaches the MHD limit as k_y decreases until $k_y < 0.1$ where there is a slight uptick in $\beta_{\rm crit}^{\rm KBM}$. The HSX curve is well below the MHD limit in the transport-relevant $k_y < 0.25$ range, and dips to values $\approx 0.1\%$ that are an order of magnitude smaller than $\beta_{\rm crit}^{\rm MHD}$. This suggests that conditions in HSX are more conducive to KBM excitation due to ion kinetic physics (see Sec. 4) than they are in NCSX. As will be shown, this is associated with the low average magnetic shear in HSX.

Figure 4 shows the dominant growth rates γ and real frequencies ω as functions of k_y at a constant

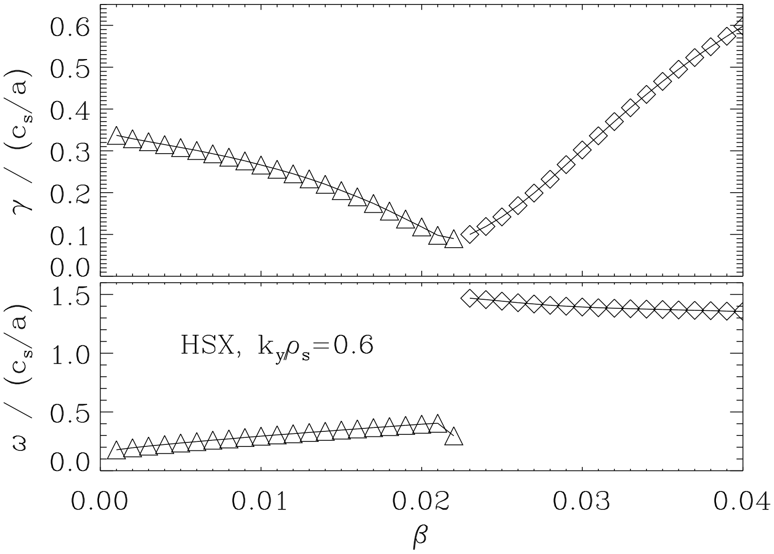

Figure 1: The growth rate and real frequency for the eigenmode with the largest growth rate at $k_y = 0.6$ over a range of β values for HSX with $a/L_{T\mathrm{i}} = 3$ and $a/L_{T\mathrm{e}} = a/L_n = T_\mathrm{i}/T_\mathrm{e} = 1$. Note the stabilization of ITG growth rates (shown as triangles) as β increases and approaches $\beta_\mathrm{crit}^\mathrm{KBM} \approx 2.2\%$, where there is a clear discontinuity in real frequency, which highlights the change in dominant mode branch from ITG to KBM (shown as diamonds).

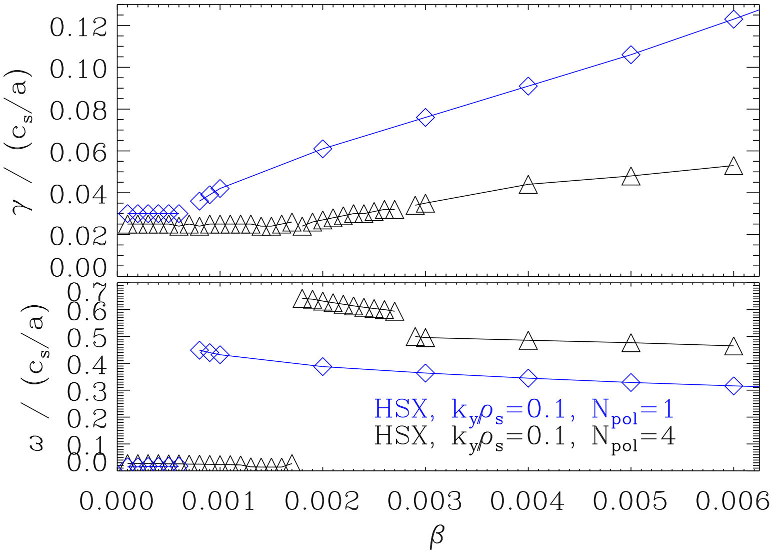

Figure 2: Growth rate and real frequency spectra for $k_y = 0.1$ of the HSX configuration with $a/L_{T\mathrm{i}} = 3$ and $a/L_{T\mathrm{e}} = a/L_n = T_\mathrm{i}/T_\mathrm{e} = 1$ for both $N_\mathrm{pol} = 1$ (blue diamonds) and $N_\mathrm{pol} = 4$ (black triangles). Note the lack of ITG stabilization relative to the $k_y = 0.6$ case and the significant difference between the two cases, an indication that $N_\mathrm{pol} = 1$ is insufficient for convergence. $\beta_\mathrm{crit}^\mathrm{KBM}$ is also much lower for this case.

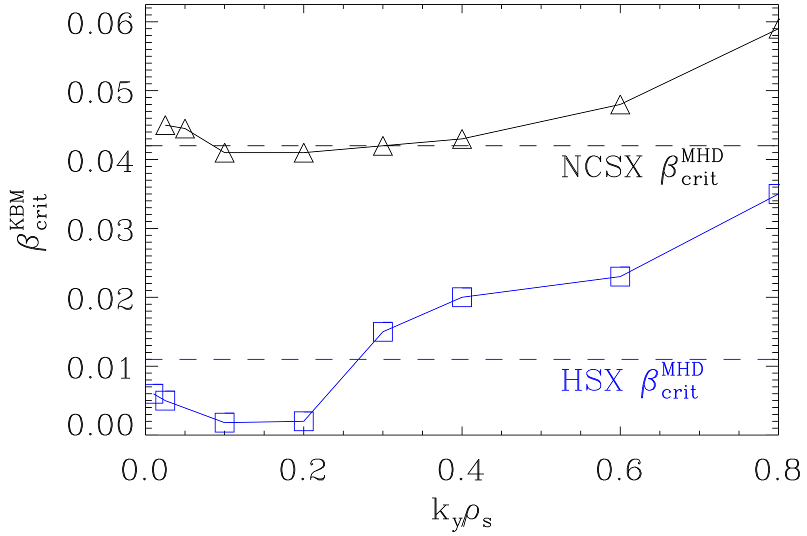

Figure 3: The $\beta_{\rm crit}^{\rm KBM}$ spectrum of NCSX (black triangles) and HSX (blue squares) with $a/L_{T{\rm i}} = 3$ and $a/L_{T{\rm e}} = a/L_n = T_{\rm i}/T_{\rm e} = 1$. Horizontal dashed lines correspond to $\beta_{\rm crit}^{\rm MHD}$. Note the low $\beta_{\rm crit}^{\rm KBM}$ relative to $\beta_{\rm crit}^{\rm MHD}$ for HSX compared to NCSX.

$\beta = 0.48\%$. It is worth noting that KBM is dominant over a certain range of k_y values, namely $k_y \in [0.1, 0.2]$, while ITG is dominant over the remainder of the wavelength range. This means that nonlinear calculations of HSX at this value of β will potentially exhibit concurrent ITG and KBM drive characteristics, a phenomenon that is also observed in nonlinear simulations of tokamaks if $\beta \geq \beta_{\rm crit}^{\rm KBM}$ [50, 52].

Lastly, the subdominant mode spectrum of HSX at $k_y = 0.2$ with $\beta = 0.5\%$, shown in Fig. 5, indicates that there is not just a single KBM that is destabilized as β increases, but rather there are two families of KBMs, one of which is a set of modes that are centred at at the outboard midplane ($\theta_p = 0$) and another which consists of pairs of sibling modes that peak away from the outboard midplane ($\theta_p \neq 0$). It should be noted that some of the centred KBMs exhibit tearing parity (blue and green curves in the bottom panel of Fig. 5), i.e., the Φ eigenfunctions are odd in ballooning angle. The low background magnetic shear in the present scenario enables destabilization of these modes, termed tearing-parity KBMs or TKBMs, which had previously been conjectured not to exist based on a study involving high-shear equilibria [49]. It is worth noting that it is unlikely that the TKBMs discussed here are micro tearing modes because of the unique ion temperature gradient dependence of the modes, the fact that the modes propagate in the ion diamagnetic direction, and the relatively small electron thermal transport nonlinearly, three qualities that

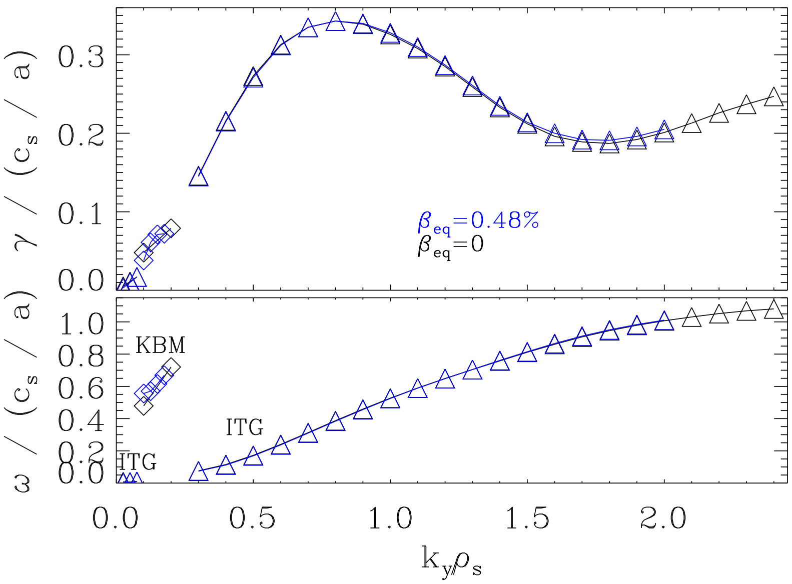

Figure 4: Growth rate and real frequency spectra for the HSX configuration (both with an equilibrium $\beta = 0$ (black) and equilibrium $\beta = 0.48\%$ (blue)) with $a/L_{T\mathrm{i}} = 3$, $\beta = 0.48\%$, and $a/L_{T\mathrm{e}} = a/L_n = T_\mathrm{i}/T_\mathrm{e} = 1$. KBMs (ITG modes) are denoted by black diamonds (triangles). Note the transition from ITG to KBM (at roughly $k_y \approx 0.1$) and back to ITG (at roughly $k_y \approx 0.2$), highlighted by the discontinuity in real frequency. Also note the similarity in the two spectra when using a finite-β magnetic equilibrium versus using the vacuum case.

are not characteristic of micro tearing modes. For each mode that peaks away from the outboard midplane a sibling mode exists with the same growth rate and frequency with an eigenmode structure that is near-perfectly mirrored with respect to $\theta_p = 0$. The physics implication of this is that HSX is qualitatively different than typical high-$\hat{s}$ tokamak cases, where only a single KBM is destabilized. Eigenvalue calculations with different gradients, $a/L_{T\mathrm{i}} = 4$ for example (with a/L_n and $a/L_{T\mathrm{e}}$ kept fixed), also exhibit the two branches of KBMs. However, the exact location of minimal $\beta_{\mathrm{crit}}^{\mathrm{KBM}}$ shifts in k_y-space relative to the $a/L_{T\mathrm{i}} = 3$ case. The region of k_y-space in which the outboard-midplane-peaked KBMs are dominant shifts to smaller k_y as $\omega_{T\mathrm{i}}$ increases. It should also be noted that the two branches of KBM are robustly present when ensuring numerical convergence. This also complicates analysis of the nonlinear energy dynamics, as there may be a number of unstable KBMs involved in nonlinear energy transfer.

3.2 Nonlinear characteristics of the ITG-KBM system

Previous studies of KBM instability and turbulence have found critical β values on the order of one or a few percent for experimentally-relevant gradient values and magnetic geometries [30, 50, 52]. These analyses

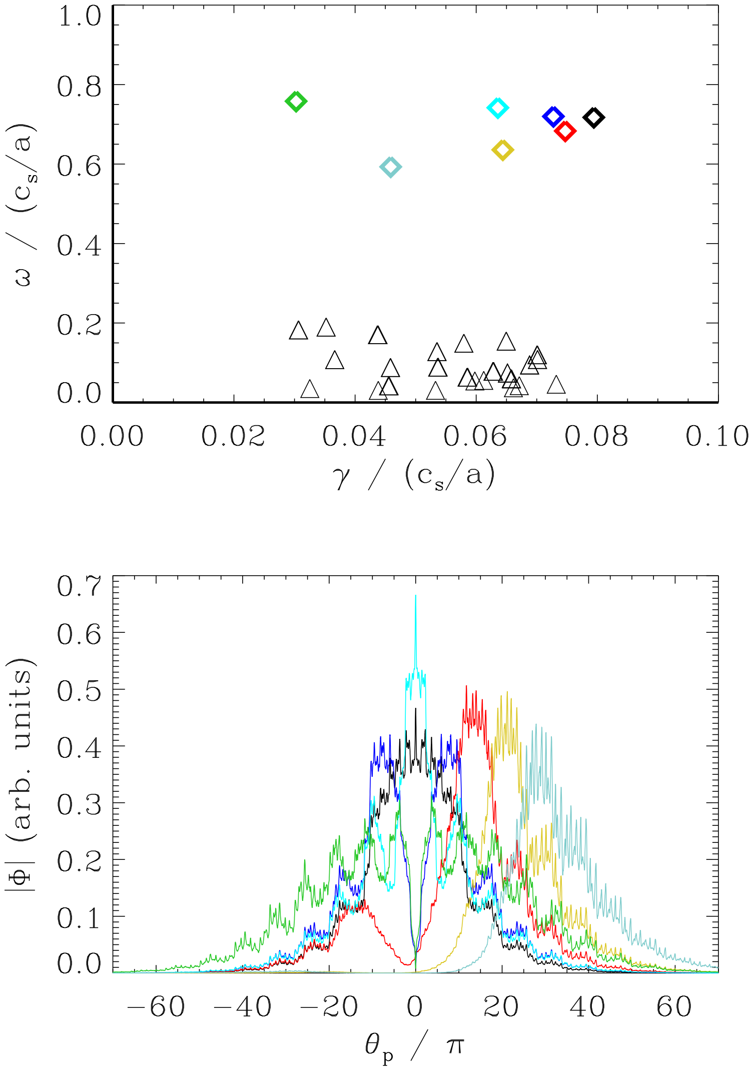

Figure 5: The subdominant spectrum (top) for HSX with $k_y = 0.2$ and $\beta = 0.5\%$ consisting of KBMs (diamonds) and ITG modes (triangles), and the associated electrostatic potential Φ eigenmode structures (bottom) for various KBMs. Note the two distinct families of KBMs: one with Φ symmetric about $\theta_p = 0$ and one with off-centre peaking. For each mode of the latter family, there is a sibling mode that is mirrored across the $\theta_p = 0$ axis with identical γ and ω, hence they are indistinguishable in the top panel. Also note that some of the centred KBMs (blue, green) have tearing parity, i.e., are odd functions of ballooning angle.

also show that for $\beta < \beta_{\text{crit}}^{\text{KBM}}$, the resulting turbulence is solely ITG or TEM and for $\beta > \beta_{\text{crit}}^{\text{KBM}}$, signatures of multiple modes are present and observable in the simulations concurrently. Contrary to these cases, when $\beta > \beta_{\text{crit}}^{\text{KBM}}$, nonlinear simulations of the present HSX case do not achieve saturation when the minimum binormal wavenumber $k_y^{\min}$ of the system is unstable to KBMs. In such simulations, streamer modes span the length of the periodic radial domain, regardless of how large the radial box is, and self-reinforce via the radial periodic boundary condition of the flux tube. However, if one chooses $k_y^{\min}$ so that it is stable to KBMs, saturation can be achieved in electromagnetic flux-tube simulations, where a significant reduction in transport is observed relative to the near-electrostatic ($\beta = 0.05\%$) case. The time traces of heat flux (both ion electrostatic and electron electromagnetic) and particle flux for $k_y^{\min} = 0.025$ are shown in Fig. 6. Despite KBM being an electromagnetic mode, below the threshold it does not drive significant electromagnetic flutter heat transport given the choice of small electron temperature gradient $a/L_{T\text{e}} = 1$. While the condition that the smallest finite k_y must be KBM-stable is empirical, one possible underlying cause is the ability of the system to terminate an inverse cascade by means of ITG (stable) eigenmodes. The precise nature of the phenomenon is left for future study.

The heat flux spectrum given in Fig. 7 shows that the ion electrostatic heat flux $Q_{\text{i}}^{\text{es}}(k_y)$ peaks in the k_y-range that is dominated by KBMs, consistent with the fact that β is roughly three times as large as $\beta_{\text{crit}}^{\text{KBM}}$ for $k_y = 0.1$. Figure 7 also shows that KBM transport is the dominant physics mechanism nonlinearly as long as KBMs are destabilized linearly, even if KBM growth rates are subdominant, where linear destabilization is shown in Fig. 4. As discussed above, $k_y^{\min}$ is sufficiently small that no KBM instability occurs at that mode; this is consistent with findings in high-$\hat{s}$ scenarios where nonlinear saturation is possible for β values up to $\beta_{\text{crit}}^{\text{KBM}}$ as $k_y \to 0$ [50]. The nonlinear electrostatic potential Φ spectrum is shown in Fig. 8, showing that the simulation is not dominated by a zonal flow, as the $k_y = 0.1$ non-zonal component of Φ is nearly a factor of two larger than the zonal component and the sum of the non-zonal contributions is significantly larger than the zonal contribution. This is an indication that zonal flows may play at most a minor role in saturation. This view is refined, however, based on nonlinear energy transfer analysis.

Nonlinear frequencies are shown in Fig. 9. Interestingly, there is no discontinuity in the nonlinear frequency spectrum of the HSX configuration, a feature that was present linearly at the ITG-KBM transition

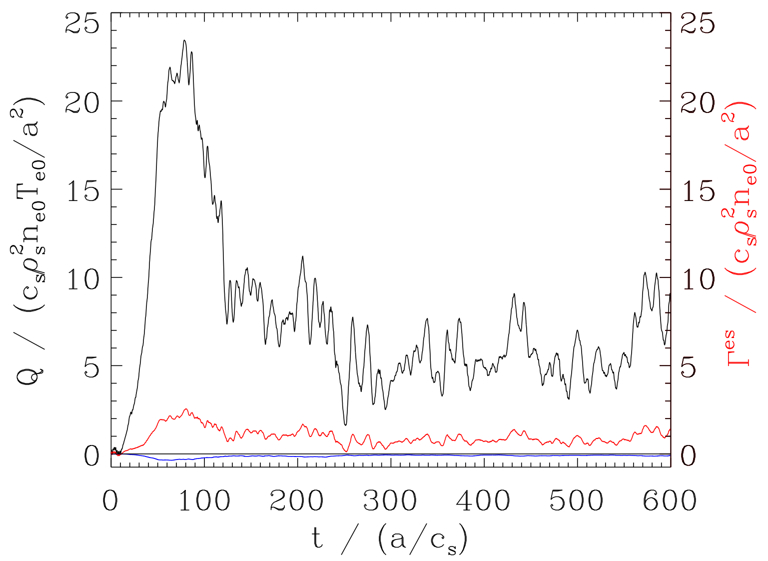

Figure 6: Heat (both ion electrostatic (black) and electron electromagnetic (blue)) and particle flux (red) time traces for HSX with $k_y^{\min} = 0.025$ and $\beta = 0.48\%$. There is a significant (factor of ≈ 5) reduction in $Q_{\mathrm{i}}^{\mathrm{es}}$ relative to the near-electrostatic ($\beta \approx 0.05\%$) case [38]. There is negligible, slightly negative magnetic flutter transport, a result of the low electron temperature gradient $a/L_{T\mathrm{e}} = 1$.

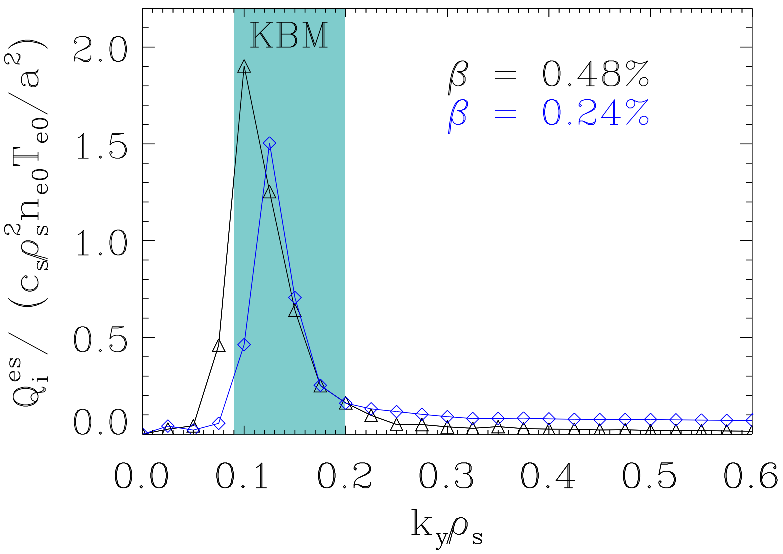

Figure 7: Heat flux spectra for HSX with $k_y^{\min} = 0.025$ and $\beta = 0.48\%$ (black) associated with the time trace shown in Fig. 6 and with $k_y^{\min} = 0.025$ and $\beta = 0.24\%$ for comparison. Note that the peaks of the spectra are almost fully contained in the binormal wavelength range over which KBM is destabilized, which is denoted by the shaded region. This shows that KBM transport dominates nonlinearly when KBMs are linearly destabilized, even if KBM growth rates are subdominant to ITG growth rates.

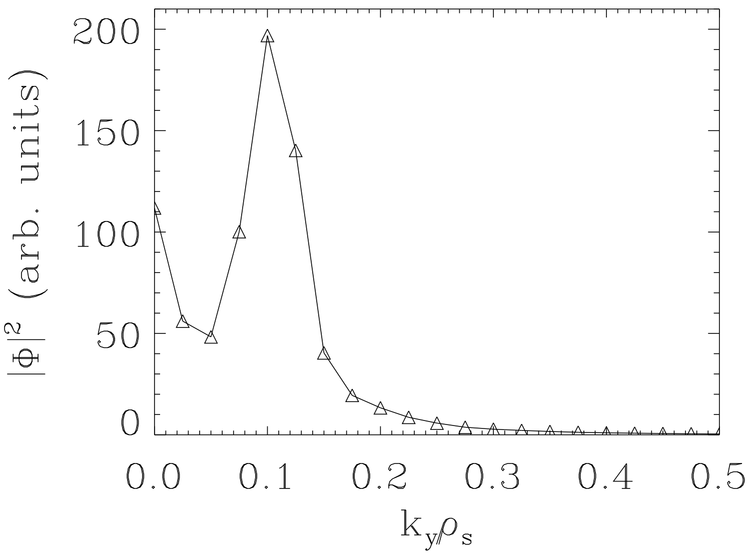

Figure 8: The nonlinear Φ spectrum for HSX with $k_y^{\min} = 0.025$ and $\beta = 0.48\%$. The spectrum is truncated at $k_y \rho_s = 0.5$ since $|\Phi|^2$ amplitudes are negligible above this threshold. Note that the zonal component is much weaker than the integrated non-zonal amplitudes.

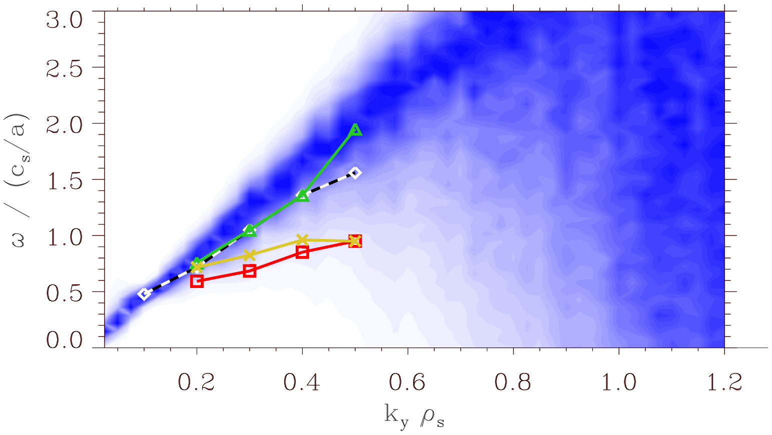

Figure 9: The nonlinear frequency spectrum for HSX with $k_y^{\min} = 0.025$ and $\beta = 0.48\%$. The colour scale has arbitrary units and is linear and normalized at each k_y separately. Linear frequencies of the most unstable (gold crosses), maximal-frequency (green triangles), minimal-frequency (red squares), and most unstable outboard-centred (black-white dashed diamonds) KBMs are also included for comparison. Note the agreement between the dominant linear outboard-centred KBM frequencies and the nonlinear signal.

points in Fig. 4. Both dominant and subdominant linear KBM frequencies are overlaid in Fig. 9 to facilitate comparison with the nonlinear data. Clearly, throughout the range where linear data is shown, nonlinear frequency signatures match the values associated with the dominant outboard-centred KBMs. An exact frequency match is not expected to occur, as turbulence may result in a k_y-dependent nonlinear frequency shift and broadening. This constitutes evidence that KBMs do indeed play an important role in the nonlinear turbulent state.

Analysis of the nonlinear energy transfer to a given (k_x,k_y) point in Fourier space due to interaction with (k'_x,k'_y) and ($k_x - k'_x, k_y - k'_y$) also suggests that modes in the KBM-dominated k_y range play an important role in the energy transfer dynamics of the turbulence and therefore in the dynamics that lead to saturation. Figure 10 shows nonlinear energy transfer at a given ($k_x = 0.06$, $k_y = 0.1$), denoted by the tip of the black arrow, to and from various (k'_x, k'_y). Regions of blue correspond to locations which cause energy input into ($k_x = 0.06$, $k_y = 0.1$) while red regions correspond to locations which draw energy from ($k_x = 0.06$, $k_y = 0.1$). The dominant method by which ($k_x = 0.06$, $k_y = 0.1$) receives energy is zonal energy transfer, indicated by the blue clouds at both $k'_y = 0$ and $k'_y = 0.1$. There is also significant non-zonal energy transfer via ($k'_x = 0.12$, $k'_y = -0.025$). It is important to note both that the largest energy sinks are due to non-zonal transfer and that the largest energy sinks are even larger than the largest energy inputs from zonal transfer. Lastly, the zonal energy transfer can occur due to both the zonal flow and the zonal field, i.e., the zonal component of the fluctuating magnetic field.

This result appears to contradict the earlier finding in Fig. 8 that the zonal-flow amplitudes are low. However, when coupling is sufficiently resonant, zonal flows can very efficiently mediate energy transfer even if they are only excited to low amplitudes.

Further analysis of nonlinear energy transfer yields insight into the wavelength ranges which dominate energy transfer between the turbulence and the zonal ($k_y = 0$) modes. Fig. 11 shows normalized nonlinear energy transfer corresponding to $k_y = 0$ modes summed over both k_x and k'_x versus k'_y. The peak of the data occurs at $k'_y = 0.125$, well within the KBM-dominated k_y-range. A significant portion of the energy transfer to and from zonal modes is facilitated by modes in the KBM-dominated k_y-range, constituting additional evidence that KBMs are important nonlinearly. One can also construct a quantity to gauge the relative

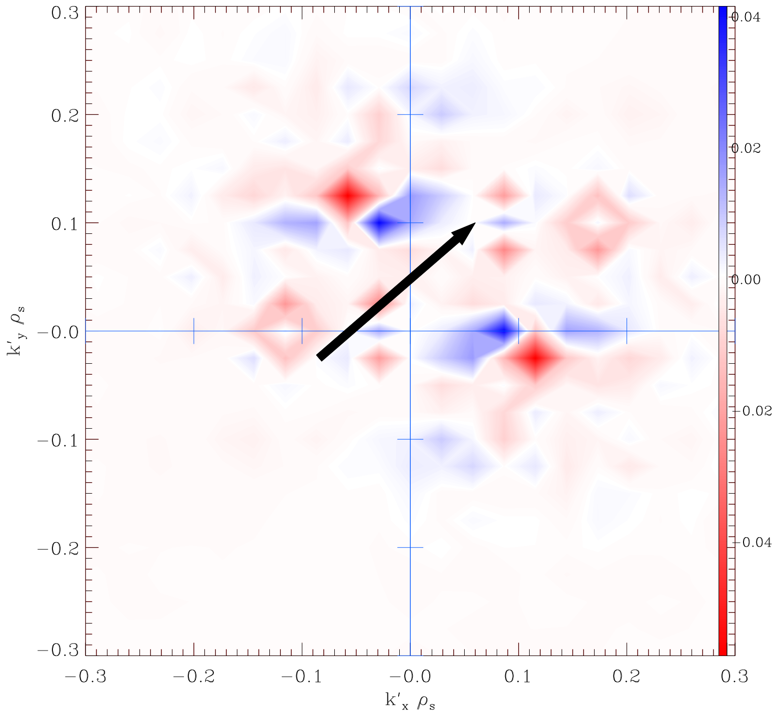

Figure 10: Nonlinear energy transfer functions indicate locations which give (blue) and receive (red) energy to and from ($k_x = 0.06$, $k_y = 0.1$), denoted by the tip of the black arrow. There is significant zonal transfer from ($k_x = 0.06$, $k_y = 0.1$) to the blue clouds near $k'_y = 0$ and $k'_y = 0.1$. Significant non-zonal energy transfer is also observed at $k'_y = -0.025$ and $k'_y = 0.125$.

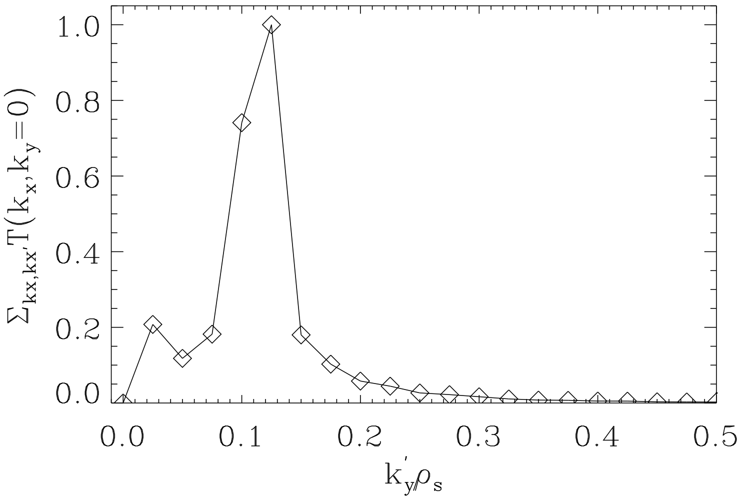

Figure 11: The sum (over $k_x \neq 0$) of the root-mean-squares (over coupled k'_x) of time-averaged nonlinear energy transfer functions for zonal ($k_y = 0$) modes as a function of k'_y. The data is normalized to the value of the point at $k'_y = 0.125$. Note that the peak is in the KBM-dominated k'_y-range, evidence that KBMs play an important role in zonal dynamics.

importance of a given k_y in the overall nonlinear energy transfer dynamics, as highlighted by Fig. 12, a plot of averaged nonlinear energy transfer functions versus k_y. This quantity is the sum (over $k_x \neq 0$) of the root-mean-squares (of each k'_x-k'_y plane) of the nonlinear energy transfer functions corresponding to a given (k_x,k_y). Both the zonal and KBMs contribute to the overall nonlinear energy transfer dynamics, with KBMs contributing roughly twice as much if one integrates over the entire KBM-dominated k_y-range.

Lastly, figure 13 shows both the electrostatic ion heat and particle fluxes as β increases. Simulations with $k_y^{\rm min} = 0.025$ for $\beta = 0.75\%$ and 1% grow without bounds and therefore do not have associated data points. This is consistent with the requirement that $k_y^{\rm min}$ be stable to KBMs for saturation to occur, as $\beta_{\rm crit}^{\rm KBM} \approx 0.6\%$ for $k_y = 0.025$, as shown in Fig. 3. Note the decrease in heat flux as β increases until β is sufficiently close to the $\beta_{\rm crit}^{\rm KBM}(k_y^{\rm min})$, a result that is consistent with ITG nonlinear finite-β stabilization. The uptick in $Q_{\rm i}^{\rm es}$ as β increases from 0.48% to 0.55% is an expression of the KBMs, which, unlike the ITG modes, become more virulent as β is increased.

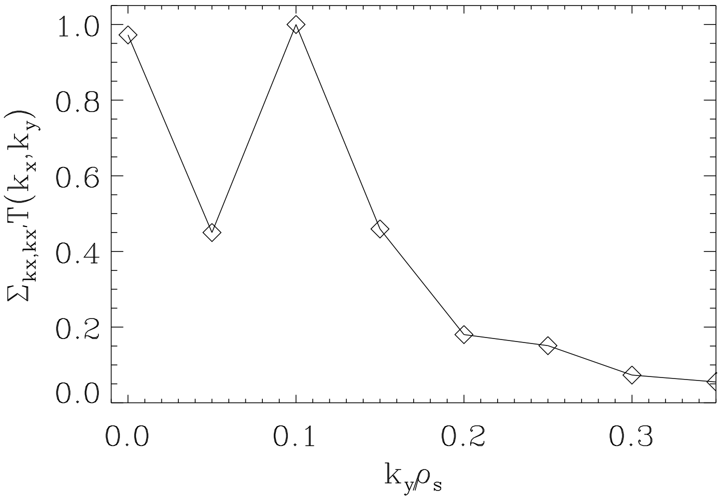

Figure 12: The sum (over $k_x \neq 0$) of the root-mean-squares (over coupled k_x', k_y') of time-averaged nonlinear energy transfer functions, which are normalized by the value of the same quantity at $k_y = 0.1$.

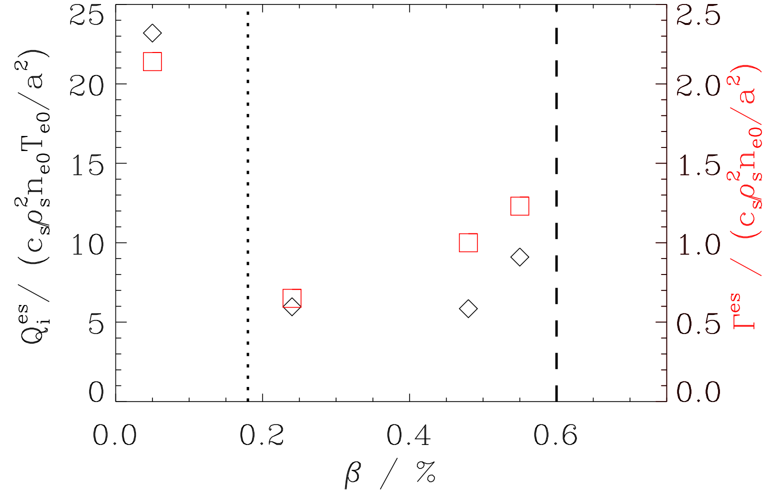

Figure 13: Normalized ion heat flux Q_i^{es} (black diamonds) and particle flux Γ^{es} (red squares) as a function of β. Observe the significant reduction of transport for $\beta \gtrsim 0.2\%$ relative to $\beta \approx 0.05\%$ until β approaches the $\beta_{crit}^{KBM} \approx 0.6\%$ threshold for $k_y = 0.025$. Above $\beta = 0.6\%$, simulations no longer achieve a saturated state. A vertical dashed black line indicates $\beta_{crit}^{KBM} = 0.6\%$ at $k_y = 0.025$ and a vertical dotted black line indicates the $\beta_{crit}^{KBM} = 0.18\%$ at $k_y = 0.1$. The electron electromagnetic heat flux is negligible (normalized $Q_e^{em} \approx -0.2$ for $\beta = 0.48\%$) and therefore not included in this analysis.

4 Impact of average magnetic shear and ion temperature gradient

Further investigation demonstrates that $\hat{s}$ and $a/L_{T\mathrm{i}}$ are particularly important in setting the value of $\beta_{\mathrm{crit}}^{\mathrm{KBM}}$ relative to the ideal ballooning threshold. This section addresses how the linear KBM characteristics presented in Section III change as both the average magnetic shear $\hat{s}$ and the fractional component of the total pressure gradient a/L_p driven by the ion temperature gradient $a/L_{T\mathrm{i}}$ change. Linear results pertaining to H-J and a circular geometry with low $\hat{s}$ will also be shown.

Figure 14 presents $\beta_{\mathrm{crit}}^{\mathrm{KBM}}$ as a function of $\hat{s}$ and demonstrates that the KBM threshold increases with $|\hat{s}|$, regardless of sign. This is consistent with the observations that, in general, drift waves are commonly stabilized by increased $|\hat{s}|$ [46, 54]. Modification of the average magnetic shear of the flux tube is done self-consistently in the sense that the derivative of $\iota\!\!\!-$ is adjusted to yield the desired $\hat{s}$ and then geometric elements are recalculated accordingly. Furthermore, eigenvalue calculations of HSX with artificially high $\hat{s}$ yield a subdominant mode spectrum that corresponds to the usual tokamak, single-unstable-KBM scenario, as well as to the NCSX configuration discussed in Sec. 3.1. The physics implication of this result is that with increased shear, modes are less extended along the magnetic field line and therefore cannot access free energy in gradients via the bad-curvature regions further along the field line, as evidenced by Fig. 15, a plot of two characteristic Φ eigenmodes for the $\hat{s} = -0.05$ case (black) and the $\hat{s} = 0.5$ case (blue). Conversely, KBMs are therefore more easily destabilized with more free energy to access when $|\hat{s}|$ is low like in HSX.

This result is consistent with previous work investigating KBM behavior in low-magnetic-shear tokamaks [24, 25, 67]. In Ref. [24], despite low negative $\hat{s}$, which implies stability with respect to ideal MHD ballooning modes, one observes KBMs at relatively small critical $\beta_{\mathrm{crit}}^{\mathrm{KBM}} \approx 0.5\%$ with $\hat{s} = -0.2$ and $k_y = 0.1$ when a sufficiently strong ion temperature gradient is present. It has been suggested that the cause of this destabilization of KBMs at small β is an ion-magnetic-drift-resonance effect [10, 24, 25]. Thermal ions couple to and exchange energy with the drift wave via the geodesic curvature of the magnetic geometry. There are also recent reports of KBMs in experiments which exhibit low negative magnetic shear [9, 10], where it is suggested that the same ion-magnetic-drift effect is responsible for the destabilization at small β.

A preliminary, lowest-order analysis of the ion-magnetic-drift resonance condition, derived using a two-fluid model which accounts for kinetic effects, given in Ref. [24]:

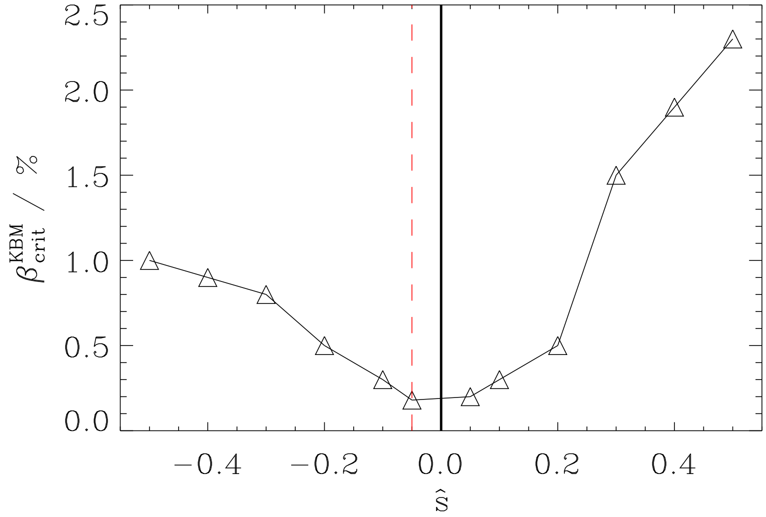

Figure 14: The $\beta_{\mathrm{crit}}^{\mathrm{KBM}}$ as a function of $\hat{s}$ for the HSX configuration with $k_y = 0.1$. A dashed vertical red line highlights the self-consistent nominal $\hat{s}$ for HSX at $s_0 = 0.5$. Note that $\beta_{\mathrm{crit}}^{\mathrm{KBM}}$ increases as the magnitude of the average magnetic shear increases, regardless of sign.

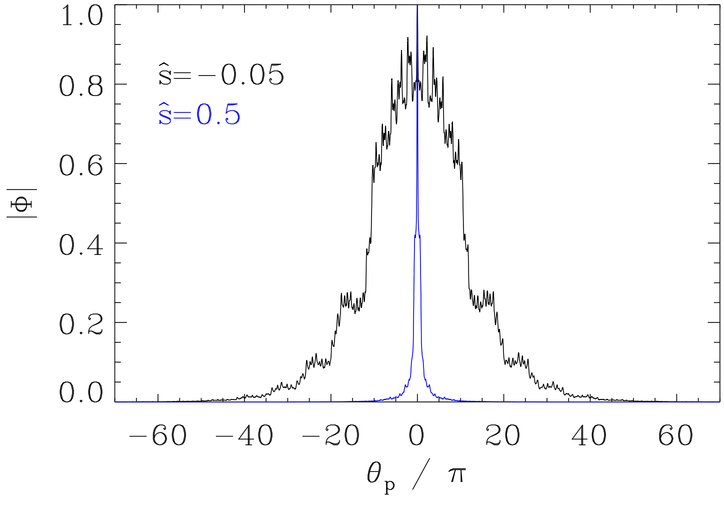

Figure 15: Characteristic Φ eigenmode structures for KBMs for the HSX geometries with $\hat{s} = -0.05$ (black) and $\hat{s} = 0.5$ (blue) which highlight the extended nature of the eigenmodes when the magnitude of the average magnetic shear is low. The mode structure magnitudes are normalized to their values at the outboard midplane.

$$(\omega - 5/3\,\omega_{D\mathrm{i}})^2 - 10/9\,\omega_{D\mathrm{i}}^2 = 0, \tag{1}$$

where $\omega_{D\mathrm{i}} = 2cT_\mathrm{i}/(eB^3)(\nabla B \times \mathbf{B}) \cdot \mathbf{k}_\perp$, suggests that the KBM frequencies observed in the present work exhibit good agreement with that which is required for exact resonance. Note the different sign used in the parenthetical in Eq. 1 due to the difference in sign convention used for ω here relative to Ref. [24]. Taking $T_e/T_\mathrm{i} = 1$, $2cT_\mathrm{i}/(eB) \to c_\mathrm{s}\rho_\mathrm{s}$, and $\nabla B \to B/a$, the ion-magnetic-drift frequency can be written as $\omega_{D\mathrm{i}}/(c_\mathrm{s}/a) \approx k_\perp\rho_\mathrm{s}$. After computing an eigenmode average for $k_\perp\rho_\mathrm{s}$ which accounts for geometry, given by

$$\langle k_\perp\rho_\mathrm{s}\rangle = \frac{\int |\Phi|^2((k_x\rho_\mathrm{s})^2 g^{xx} + 2k_xk_y\rho_\mathrm{s}^2 g^{xy} + (k_y\rho_\mathrm{s})^2 g^{yy})^{1/2} d\theta_p}{\int |\Phi|^2 d\theta_p}, \tag{2}$$

where g^{xx}, g^{xy}, and g^{yy} are magnetic geometry elements, $\omega_{D\mathrm{i}}/(c_\mathrm{s}/a) \approx \langle k_\perp\rho_\mathrm{s}\rangle$ yields a normalized ion-magnetic-drift frequency $\omega_{D\mathrm{i}} = 0.266$ for $(k_x = 0,\ k_y = 0.2)$. Using this value for $\omega_{D\mathrm{i}}$, one can evaluate Eq. 1 to determine the resonant mode frequency. The resonant frequency is $\omega \approx 0.724$ for $(k_x = 0,\ k_y = 0.2)$. The resonant frequency calculated here is in agreement with the dominant KBM real frequency in Fig. 4 at $k_y = 0.2$, where $\omega_r \approx 0.72$. This constitutes quantitative evidence that the ion magnetic drift resonance is likely playing an important role in the dynamics. A more thorough analysis of the ion-magnetic-drift resonance phenomenon will be left to future work.

In support of the concept that ion dynamics are of particular importance to KBM behavior in HSX geometry, Fig. 16 shows $\beta_\mathrm{crit}^\mathrm{KBM}$ as a function of k_y, similar to Fig. 3, but with different gradients. Keeping the sum of the gradients as well as $a/L_{T\mathrm{e}}$ constant, setting $a/L_{T\mathrm{i}} = 0$, and increasing $a/L_{T\mathrm{n}}$ accordingly, one observes both roughly an eight-fold increase in $\beta_\mathrm{crit}^\mathrm{KBM}$ at $k_y = 0.1$ and that $\beta_\mathrm{crit}^\mathrm{KBM}$ no longer dips as far below $\beta_\mathrm{crit}^\mathrm{MHD}$. Below $k_y = 0.025$, $\beta_\mathrm{crit}^\mathrm{KBM}$ is difficult to ascertain, as a mode which drifts in the electron diamagnetic direction with even Φ-parity and odd $A_\parallel$-parity dominates over the relevant β range and eigenvalue calculations are impractical at such small values of k_y. This result constitutes further evidence that ion dynamics are of particular importance to KBM behavior in HSX.

Regarding scalings of KBM turbulence and confinement at high β, linear computations alone are often insufficient to predict nonlinear trends, particularly at low $\hat{s}$, as discussed in, e.g., [23, 38]. While

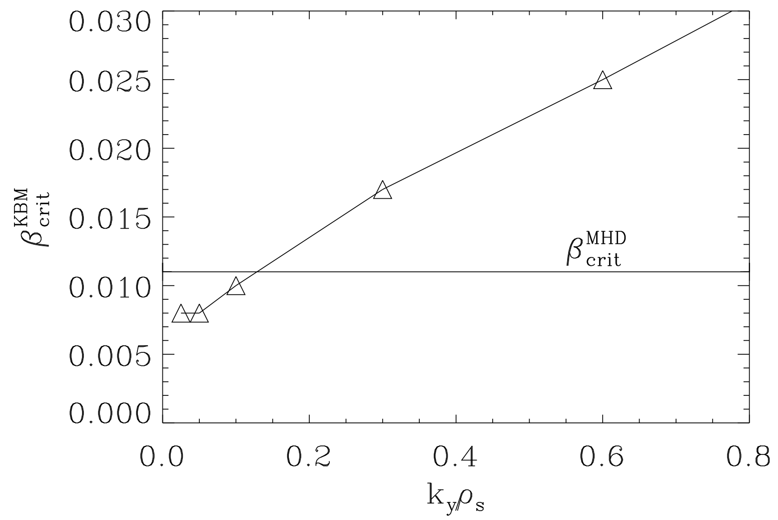

Figure 16: The $\beta_{\rm crit}^{\rm KBM}$ spectrum for HSX with a stronger density gradient contribution compared with Fig. 3: $a/L_n = 2.5$, $a/L_{T\rm i} = 0$, and $a/L_{T\rm e} = 1$. Since two particle species are used, the sum of the gradients is $2.5 + 2.5 + 1 = 6$, which is equal to the sum of the gradients in Fig. 3. Note that the KBM limit is now closer to $\beta_{\rm crit}^{\rm MHD}$ as $k_y \to 0$.

more research on this topic in the context of KBMs is required, the low heat fluxes in Fig. 6 show both that the strong linear KBM drive at low magnetic shear does not produce corresponding fluxes and that electromagnetic stabilization of the heat flux relative to the electrostatic case can be shown. More explicitly, dominant linear growth rates alone are poor predictors of nonlinear heat fluxes at finite β.

Analyses similar to the ones conducted above for HSX were also carried out for both Heliotron-J and a circular axisymmetric geometry. H-J, a configuration with similarly low average magnetic shear ($\hat{s} \approx 0.028$), also exhibits a small $\beta_{\rm crit}^{\rm KBM} \approx 0.14\%$ at $k_y = 0.1$, as evidenced by Fig. 17. This value of $\beta_{\rm crit}^{\rm KBM}$ verifies calculations carried out using the GKV code of the same H-J equilibrium using the same gradient values [29, 37]. Also note that there is a slight increase in the ITG growth rates as $\beta \to \beta_{\rm crit}^{\rm KBM}$, i.e., no linear electromagnetic stabilization occurs. One particular benefit of including H-J in this analysis is to highlight the fact that the linear and nonlinear KBM dynamics observed numerically in HSX are not simply the product of an aspect of the magnetic geometry that is unique to HSX, but rather are indicative of KBM behavior in a broader class of magnetic equilibria which exhibit small average magnetic shear.

A shifted-circle tokamak geometry with a low negative average magnetic shear $\hat{s} \approx -0.05$ also exhibits similar $\beta_{\rm crit}^{\rm KBM}$ spectra and eigenvalue characteristics to those for HSX, as shown in Fig. 18. Note

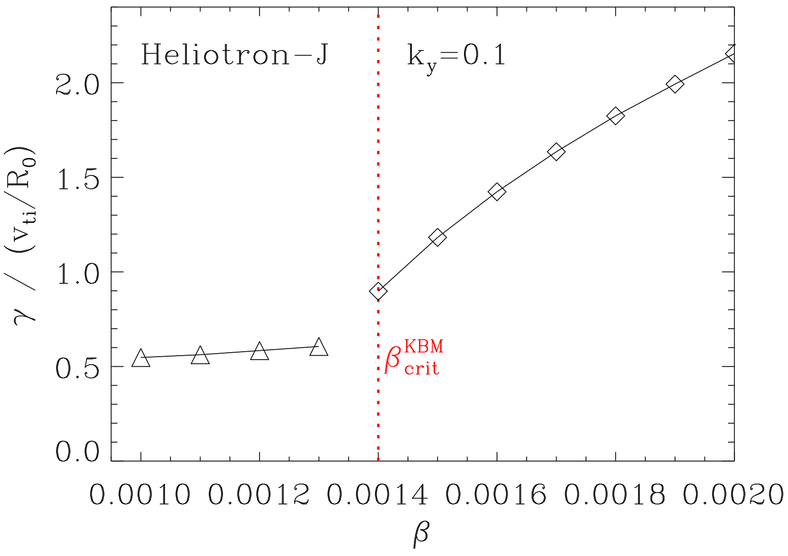

Figure 17: Growth rate γ as a function of β for H-J at $k_y = 0.1$ with the following normalized (to major radius) gradients: $R_0/L_{T\rm i} = 13$, $R_0/L_{T\rm e} = 17$, and $R_0/L_n = 9.3$. ITG modes (triangles) dominate below $\beta_{\rm crit}^{\rm KBM}$ and KBMs (diamonds) dominate above $\beta_{\rm crit}^{\rm KBM}$. Note that $\beta_{\rm crit}^{\rm KBM} = 0.14\%$, shown in red, is comparable to HSX for the same binormal wavenumber.

the similarities in the $\beta_{\rm crit}^{\rm KBM}$ spectrum between HSX and the circular tokamak with low negative average magnetic shear. Both curves are non-monotonic and have a minimum at $k_y = 0.1$ with a very small critical $\beta_{\rm crit}^{\rm KBM} \approx 0.1\%$, as shown in the top panel of Fig. 18. It is also worth noting that the low-k_y behavior of $\beta_{\rm crit}^{\rm KBM}$ in s-α is insensitive to the use of a self-consistent equilibrium relative to the high-k_y behavior. The subdominant mode landscape for the circular tokamak is also qualitatively consistent with the HSX results, as two distinct clouds of modes are present, an ITG and a KBM branch, as shown in Fig. 18. However, one key difference between the subdominant mode spectra for HSX and the circular tokamak is the presence of only a single ballooning-parity and tearing-parity KBM branch for the circular tokamak case. The single KBM branch in the axisymmetric case resembles the branch of KBMs centred at the outboard midplane for HSX.

In summary, both Heliotron-J and a circular axisymmetric geometry with $\hat{s} \approx -0.05$ exhibit KBM behavior similar to that in HSX, providing strong evidence that the relatively weak averaged magnetic shear is an important factor in determining the KBM dynamics.

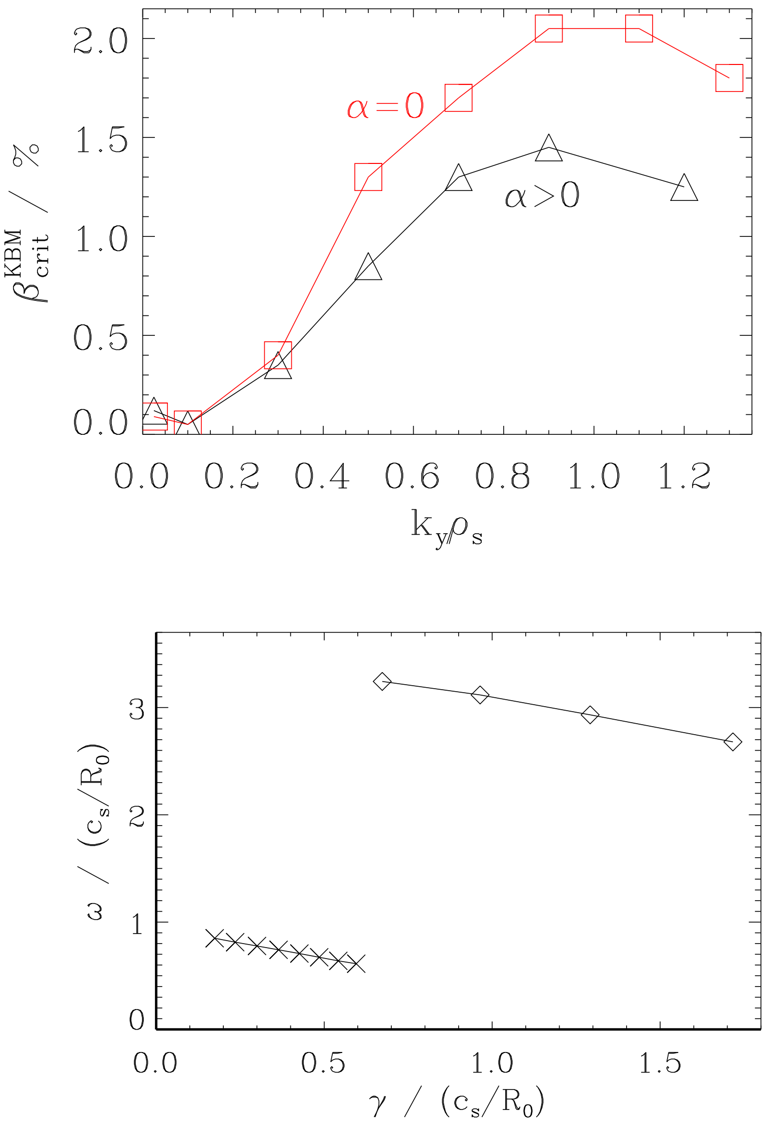

Figure 18: The $\beta_{\rm crit}^{\rm KBM}$ spectrum (top) and the subdominant mode spectrum at $k_y = 0.2$ and $\beta = 0.8\%$ (bottom) for an $\hat{s} = -0.052$ circular tokamak (s-α) geometry. The top figure contains two curves, one for the case when $\alpha_{\rm MHD} = 0$ (red squares), the equilibrium and GENE β are not self-consistent, and a second for the case when $\alpha_{\rm MHD}$ is such that both the equilibrium and GENE β are the same (black triangles). Regarding the bottom figure, the two distinct subdominant ITG (X) and kinetic ballooning mode (diamonds) clouds are also present in the circular tokamak case. However, there is only a single KBM branch in this case versus the two that were present in HSX.

5 Conclusions

Gyrokinetic electromagnetic simulations of HSX, H-J, and a circular tokamak have been presented, showing that kinetic ballooning modes can be excited at a critical $\beta_{\mathrm{crit}}^{\mathrm{KBM}}$ that is considerably smaller than the critical β for ideal MHD ballooning. This difference is associated with the relatively low average magnetic shear of these configurations. While one might expect this to bode poorly for the performance of low-average-shear magnetic equilibria, nonlinear simulations of HSX show that saturation is achievable with $\beta_{\mathrm{crit}}^{\mathrm{KBM}} < \beta < \beta_{\mathrm{crit}}^{\mathrm{MHD}}$ and that a significant reduction in transport is observed relative to the $\beta \approx 0$ case. However, saturation only occurs when the minimum binormal wavenumber $k_y^{\mathrm{min}}\rho_{\mathrm{s}}$ of the system is stable to KBMs. One possible explanation of this result is that the nonlinear transfer of energy from the strongly driven KBMs in the binormal wavenumber range $0.1 < k_y\rho_{\mathrm{s}} < 0.2$ to stable modes with $k_y\rho_{\mathrm{s}} < 0.1$ in Fourier space is possible and allows for saturation when the condition that $k_y^{\mathrm{min}}\rho_{\mathrm{s}}$ is stable to KBMs is met.

The KBM subdominant mode spectrum of HSX is qualitatively different than what one would observe in a $\hat{s} \sim 1$ tokamak, as HSX exhibits two families of unstable KBMs, whereas there is generally only a single unstable KBM in the high-$\hat{s}$ tokamak case. With low $\hat{s}$, KBMs are more extended along the field line, allowing such modes to access free energy in the gradients via the bad curvature regions away from the outboard midplane of a given field line. As a consequence, KBMs can peak at finite ballooning angle, and even tearing-parity KBMs (TKBMs in the nomenclature of Ref. [49]) are found. With respect to $\hat{s}$, $\beta_{\mathrm{crit}}^{\mathrm{KBM}}$ increases monotonically, regardless of the sign of the average magnetic shear. This is consistent with the fact that stronger magnetic shear tends to stabilize drift waves.

A number of nonlinear analyses have also been conducted here which highlight the importance of KBMs in the nonlinear dynamics. Heat flux spectra shown in Fig. 7 highlight that KBM transport dominates the dynamics when KBMs are destabilized linearly, even if KBM growth rates are subdominant to ITG growth rates. A comparison of dominant linear KBM real frequencies and nonlinear frequencies shows good agreement in the KBM-dominated k_y-range. This constitutes evidence that KBMs are significantly contributing to the nonlinear state. Additionally, an analysis of nonlinear energy transfer shows that KBMs play an integral role in the energy transfer dynamics, even more so than zonal modes, further highlighting the fact that the nonlinear state indeed shows signs of both ITG and KBM drive. An investigation of how the electrostatic ion heat flux changes as a function of β shows a decrease in heat flux as β increases until β is sufficiently close to $\beta_{\mathrm{crit}}^{\mathrm{KBM}}(k_y = k_y^{\mathrm{min}})$, showing both the improved nonlinear behavior relative to linear $\beta_{\mathrm{crit}}^{\mathrm{KBM}}$ predictions and the steep increase in fluxes at large values of $\beta \gg \beta_{\mathrm{crit}}^{\mathrm{KBM}}$.

The linear characteristics of the low-average-magnetic-shear equilibria presented in this work raise questions regarding the utility of such configurations at the β values required for an efficient fusion reactor concept. However, as the nonlinear calculations presented here show, nonlinear dynamics can overcome poor linear KBM properties such as the increase in total heat flux generally associated with $\beta > \beta_{\mathrm{crit}}^{\mathrm{KBM}}$, and nonlinear fluxes in HSX even decrease as β increases above $\beta_{\mathrm{crit}}^{\mathrm{KBM}}(k_y = 0.1)$, as shown in Fig. 13, until $\beta \approx 0.6\%$. It is important to keep such KBM saturation physics in mind during efforts to optimize stellarator equilibria at reactor-relevant β values. Lastly, the fact that in the present simulations, achieving saturation depends critically on $\beta_{\mathrm{crit}}^{\mathrm{KBM}}(k_y = k_y^{\mathrm{min}})$, it is possible that the value of $\rho^\star = \rho_{\mathrm{s}}/a$ – and thus the KBM threshold at $n = 1$ – of a low-magnetic-shear confinement device may affect the achievable plasma β. However, future investigation will need to determine whether this effect survives in more realistic simulation frameworks, in particular when retaining global profile effects.

Acknowledgements

The authors thank K. Aleynikova, M. Kotschenreuther and T.B. Cote for fruitful discussions.

Funding

This work was supported by the U.S. Department of Energy, Office of Science, Fusion Energy Sciences (award numbers DE-FG02-93ER54222, DE-FG02-04ER54742, DE-FG02-89ER53291 and DE-FG02-99ER54546). Computing time was provided through the National Energy Research Scientific Computing Center, a DOE Office of Science User Facility (grant number DE-AC02-05CH11231).

Declaration of interests

The authors report no conflict of interest.

References

[1] Aleynikova, K. and Zocco, A. 2017 Quantitative study of kinetic ballooning mode theory in simple geometry. *Phys. Plasmas* **24**, 092106.

[2] Aleynikova, K., Zocco, A., Xanthopoulos, P., Helander, P., and Nührenberg, C. 2018 Kinetic ballooning modes in tokamaks and stellarators. *J. Plasma Phys.* **84**, 745840602.

[3] Antonsen Jr., T.M., Drake., J.F., Guzdar, P.N., Hassam, A.B., Lau, Y.T., Liu, C.S., and Novakovskii, S.V. 1996 Physical mechanism of enhanced stability from negative shear in tokamaks: Implications for edge transport and the L-H transition. *Phys. Plasmas* **3** (6), 2221-2223.

[4] Antonsen Jr., T.M. and Lane, B. 1980 Kinetic equations for low frequency instabilities in inhomogeneous plasmas. *Phys. Fluids* **23**, 1205.

[5] Ball, J., Brunner, S., and Ajay, C.J. 2020 Eliminating turbulent self-interaction through the parallel boundary condition in local gyrokinetic simulations. J. Plasma Phys. **86** (2), 905860207.

[6] Boozer, A.H. 1983 Transport and isomorphic equilibria. *Phys. Fluids* **26** (2), 496-499.

[7] Brizard, A.J. and Hahm, T.S. 2007 Foundations of nonlinear gyrokinetic theory. *Rev. Mod. Phys.* **79** (2), 421-468.

[8] Canik, J.M., Anderson, D.T., Anderson, F.S.B., Likin, K.M., Talmadge, J.N., and Zhai, K. 2007 Experimental demonstration of Improved Neoclassical Transport with Quasihelical Symmetry. *Phys. Rev. Lett.* **98** (8), 085002.

[9] Chen, W., Ma, R.R., Li, Y.Y., Shi, Z.B., Du, H.R., Jiang, M., Yu, L.M., Yuan, B.S., Li, Y.G., Yang, Z.C. *et al.* 2016 Alfvénic ion temperature gradient activities in a weak magnetic shear plasma. *EPL* **116**, 45003.

[10] Chen, W., Yu, D.L., Ma, R.R., Shi, P.W., Li, Y.Y., Shi, Z.B., Du, H.R., Ji, X.Q., Jiang, M., Yu, L.M. *et al.* 2018 Kinetic electromagnetic instabilities in an ITB plasma with weak magnetic shear. *Nucl. Fusion* **58**, 056004.

[11] Cheng, C.Z. 1982 Kinetic theory of collisionless ballooning modes. *Phys. Fluids* **25**, 1020.

[12] Connor, J.W., Hastie, R.J., and Taylor, J.B. 1978 Shear, Periodicity, and Plasma Ballooning Modes. *Phys. Rev. Lett.* **40**, 396.

[13] Coppi, B. 1965 'Universal' instabilities from plasma moment equations. *Phys. Lett.* **14** (3), 172-174.

[14] Coppi, B., Rosenbluth, M.N., and Sadgeev, R.Z. 1967 Instabilities due to temperature gradients in complex magnetic field configurations. *Phys. Fluids* **10** (3), 582.

[15] Dong, J.Q., Guzdar, P.N., and Lee, Y.C. 1987 Finite beta effects on ion temperature gradient driven modes. *Phys. Fluids* **30**, 2694.

[16] Faber, B.J., Pueschel, M.J., Proll, J.H.E., Xanthopoulos, P., Terry, P.W., Hegna, C.C., Weir, G.M., Likin, K.M., and Talmadge, J.N. 2015 Gyrokinetic studies of trapped electron mode turbulence in Helically Symmetric eXperiment stellarator. *Phys. Plasmas* **22** (7), 072305.

[17] Faber, B.J., Pueschel, M.J., Terry, P.W., Hegna, C.C., and Roman, J.E. 2018 Stellarator microinstabilities and turbulence at low magnetic shear. *J. Plasma Phys.* **84** (5), 905840503.

[18] Gates, D.A., Anderson, D.T., Anderson, F.S.B., Zarnstorf, M., Spong, D.A., Weitzner, H., Neilson, G.H., Ruzic, D.N., Andruczyk, D., Harris, J.H., *et al.* 2018 Stellarator research opportunities: a report on the National Stellarator Coordinating Committee. *J. Fusion Energy* **37** (1), 51-94.

[19] Greene, J.M. and Chance, M.S. 1981 The second region of stability against ballooning modes. *Nucl. Fusion* **21**, 453.

[20] Grimm, R.C., Greene, J.M., and Johnson, J.L. 1976 Computation of the Magnetohydrodynamic Spectrum in Axisymmetric Toroidal Confinement Systems. *Meth. Comput. Phys.* **16**, 253-280.

[21] Hall, L.S. and McNamara, B. 1975 Three-dimensional equilibrium of the anisotropic, finite-pressure guilding-center plasma: Theory of the magnetic plasma. *Phys. Fluids* **18** (5), 552-565.

[22] Hegna, C.C. and Hudson, S.R. 2002 Ideal magnetohydrodynamic ballooning stability boundaries in three-dimensional equilibria. *Phys. Plasmas* **9** (5), 2014.

[23] Hegna, C.C., Terry, P.W., and Faber, B.J. 2018 Theory of ITG turbulent saturation in stellarators: identifying mechanisms to reduce turbulent transport. *Phys. Plasmas* **25** (2), 022511.

[24] Hirose, A. and Elia, M. 1996 Kinetic Ballooning Mode with Negative Shear. *Phys. Rev. Lett* **76** (4), 628.

[25] Hirose, A., Zhang, L., and Elia, M. 1995 Ion temperature gradient-driven ballooning mode in tokamaks. *Phys. Plasmas* **2**, 859.

[26] Hirsch, M., Baldzuhn, J., Beidler, C., Brakel, R., Burhenn, R., Dinklage, A., Ehmler, H., Endler, M., Erckmann, V., Feng, Y. *et al.* 2008 Major results from the stellarator Wendelstein 7-AS. *Plasma Phys. Control. Fusion* **50**, 053001.

[27] Hirshman, S.P., van Rij, W.I., and Merkel, P. 1986 Three-dimensional free boundary calculations using a spectral Green's function method. *Comput. Phys. commun.* **43** (1), 143-155.

[28] Horton, W. Jr, Choi, D.-I., and Tang, W.M. 1981 Toroidal drift modes driven by ion temperature gradients. *Phys. Fluids* **24** (6), 1077.

[29] Ishizawa, A., Kishimoto, Y., Watanabe, T.-H., Sugama, H., Tanaka, K., Satake, S., Kobayashi, S., Nagasaki, K., and Nakamura, Y. 2017 Multi-machine analysis of turbulent transport in helical systems via gyrokinetic simulation. *Nucl. Fusion* **57**, 066010.

[30] Ishizawa, A., Maeyama, S., Watanabe, T.-H., Sugama, H., and Nakajima, N. 2013 Gyrokinetic turbulence simulations of high-beta tokamak and helical plasmas with full-kinetic and hybrid models. *Nucl. Fusion* **53**, 053007.

[31] Ishizawa, A., Urano, D., Nakamura, Y., Maeyama, S., and Watanabe, T.-H. 2019 Persistence of Ion Temperature Gradient Turbulent Transport at Finite Normalized Pressure. *Phys. Rev. Lett.* **123** (2), 025003.

[32] Jarmén, A., Anderson, J., and Malinov, P. 2015 Effects of parallel ion motion on electromagnetic toroidal ion temperature gradient modes in a fluid model. *Phys. Plasmas* **22** (8), 082508.

[33] Jenko, F. 2000 Massively parallel Vlasov simulation of electromagnetic drift-wave turbulence. *Compur. Phys. Commun.* **125**, 196-209.

[34] Kadomtsev, B.B. and Pogutse, O.P. 1971 Trapped particles in toroidal magnetic systems. *Nucl. Fusion* **11**, 67-92.

[35] Kim, J.Y., Horton, W., and Dong, J.Q. 1993 Electromagnetic effect on the toroidal ion temperature gradient mode. *Phys. Fluids B* **5**, 4030.

[36] Kotschenreuther, M. 1986 Compressibility effects on ideal and kinetic ballooning modes and elimination of finite Larmor radius stabilization. *Phys. Fluids* **29** (9), 2898-2913.

[37] Maeyama, S., Ishizawa, A., Watanabe, T.-H., Nakajima, N., Tsuji-lio, S., and Tsutsui, H. 2013 Numerical techniques for parallel dynamics in electromagnetic gryokinetic Vlasov simulations. *Comput. Phys. Commun.* **184** (11), 2462-2473.

[38] McKinney, I.J., Pueschel, M.J., Faber, B.J., Hegna, C.C., Talmadge, J.N., Anderson, D.T., Mynick, H.E., and Xanthopoulos, P. 2019 A comparison of turbulent transport in a quasi-helical and a quasi-axisymmetric stellarator. J. Plasma Phys. **85**, 905850503.

[39] Mikhailov M.I., Shafranov, V.D., Subbotin, A.A., Yu. Isaev, M., Nührenberg, Zille, R., and Cooper, W.A. 2002 Improved α-particle confinement in stellarators with poloidally closed contours of the magnetic field strength. *Nucl. Fusion* **42**, L23-L26.

[40] Mynick, H.E. 2006 Transport optimization in stellarators. *Phys. Plasmas* **13** (5), 058102.

[41] Mynick, H.E., Pomphrey, N., and Xanthopoulos, P. 2010 Optimizing stellarators for turbulent transport. *Phys. Rev. Lett.* **105** (9), 095004.

[42] Neilson, G.H., Zarnstorff, M.C., Lyon, J.F., and The NCSX Team 2002 Quasi-symmetry in stellarator research 5. Status of physics design of quasi-axisymmetry stellarators 5.1 Physics design of the National Compact Stellarator Experiment. *J. Plasma Fusion Res.* **78** (3), 214-219.

[43] Nührenberg, J. and Zille, R. 1988 Quasi-helically symmetric toroidal stellarators. *Phys. Lett. A* **129** (2), 113-117.

[44] Obiki, T., Sano, F., Wakatani, M., Kondo, K., Mizuuchi, T., Hanatani, K., Nakamura, Y., Nagasaki, K., Okada, H, Nakasuga, M., *et al.* 2000 Goals and status of Heliotron-J. *Plasma Phys. Control. Fusion* **42**, 115-1164.

[45] Palumbo, D. 1968 Some considerations on closed configurations of magnetohydrostatic equilibrium. *Nuovo Cimento B* **53**, 507-511.

[46] Pearlstein, L.D. and Berk, H.L. 1969 Universal eigenmode in a strongly sheared magnetic field. *Phys. Rev. Lett.* **23** (5), 220.

[47] Pu, Y.-K. and Migliuolo, S. 1985 Finite beta stabilization of the kinetic ion mixing mode. *Phys. Fluids* **28**, 1722.

[48] Pueschel, M.J., Dannert, T., and Jenko, F. 2010 On the role of the numerical dissipation in gyrokinetic Vlasov simulations of plasma microturbulence. *Comput. Phys. Commun.* **181** (8), 1428-1437.

[49] Pueschel, M.J., Hatch, D.R., Ernst, D.R., Guttenfelder, W., Terry, P.W., Citrin, J., and Connor, J.W. 2019 On microinstabilities and turbulence in steep-gradient regions of fusion devices. *Plasma Phys. Control. Fusion* **61** (3), 034002.

[50] Pueschel, M.J. and Jenko, F. 2010 Transport properties of finite-β microturbulence. *Phys. Plasmas* **17**, 062307.

[51] Pueschel, M.J., Jenko, F., Told, D. and Buchner, J. 2011 Gyrokinetic simulations of magnetic reconnection, *Phys. Plasmas* **18** (11), 112102.

[52] Pueschel, M.J., Kammerer, M., and Jenko, F. 2008 Gyrokinetic turbulence simulations at high plasma beta. *Phys. Plasmas* **15**, 102310.

[53] Rodríguez, E., Helander P., and Bhattacharjee, A. 2020 Necessary and sufficient conditions for quasisymmetry. *Phys. Plasmas* **27** (6), 062501.

[54] Ross, D.W. and Mahajan, S.M. 1977 Are Drift-Wave Eigenmodes Unstable? *Phys. Rev.Lett.* **40** (5), 324.

[55] Rudakov, L.I. and Sagdeev, R.Z. 1961 On the instability of a nonuniform rarefied plasma in a strong magnetic field. *Dokl. Akad. Nauk SSR* **138** (3), 581-583.

[56] Snyder, P.B. 1999 Gyrofluid Theory and Simulation of Electromagnetic Turbulence and Transport in Tokamak Plasmas. PhD Thesis.

[57] Snyder P.B., Hammett G.W., Beer M.A., and Dorland, W. 1999 Simulations of Electromagnetic Turbulence and Transport in Tokamak Plasmas. *Proc. 26th EPS Conf. on Contr. Fusion and Plasmas Physics*, ECA 23J, 1685.

[58] Strauss, H.R. 1979 Finite beta trapped electron fluid mode. *Phys. Fluids* **22**, 1079.

[59] Tang, W.M. 1978 Microinstability Theory in Tokamaks. *Nucl. Fusion* **18** (8), 1089.

[60] Whelan, G.G., Pueschel, M.J., and Terry, P.W. 2018 Nonlinear Electromagnetic Stabilization of Plasma Microturbulence. *Phys. Rev. Lett.* **120**, 175002.

[61] Whelan, G.G., Pueschel, M.J., Terry, P.W., Citrin, J., McKinney, I.J., Guttenfelder, W., and Doerk, H. 2019 Saturation and nonlinear electromagnetic stabilization of ITG turbulence. *Phys. Plasmas* **26** (8), 082302.

[62] Wolf, R.C., Alonso, A., Äkäslompolo, S., Baldzuhn, J., Beurskens, M., Beidler, C.D., Biedermann, C., Bosch, H.-S., Bozhenkov, S., Brakel, R. *et al.* 2019 Performance of Wendelstein 7-X stellarator plasmas during the first divertor operation phase. *Phys. Plasmas* **26**, 082504.

[63] Xanthopoulos, P., Cooper, W.A., Jenko, F., Turkin, Y., Runov, A., and Geiger, J. 2009 A geometry interface for gyrokinetic microturbulence investigations in toroidal configurations. *Phys. Plasmas* **16** (8), 082303.

[64] Xanthopoulos, P. and Jenko, F. 2007 Gyrokinetic analysis of linear microinstabilities for the stellarator Wendelstein 7-X. *Phys. Plasmas* **14** (4), 042501.

[65] Xanthopoulos, P., Mynick, H.E., Helander, P., Turkin, Y., Plunk, G.G., Jenko, F., Görler, T., Told, D., Bird, T., and Proll, J.H.E. 2014 Controlling turbulence in present and future stellarators. *Phys. Rev. Lett.* **113** (15), 155011.

[66] Yu. Isaev, M., Nührenberg, J., Mikhailov, M.I., Cooper, W.A., Watanabe, K.Y., Yokoyama, M., Yamazaki, K., Subbotin, A.A., and Shafranov, V.D. 2003 A new class of quasi-omnigenous configurations. *Nucl. Fusion* **43**, 1066-1071.

[67] Zonca, F., Chen, L., Dong, J.Q., and Santoro, R.A. 1999 Existence of ion temperature gradient driven shear Alfvén instabilities in tokamaks. *Phys. Plasmas* **6**, 1917.